



The ensemble effect of nitrogen doping and ultrasmall SnO₂ nanocrystals on graphene sheets for efficient electroreduction of carbon dioxide

Baohua Zhang^a, Zhihao Guo^a, Zhuang Zuo^a, Wei Pan^b, Jintao Zhang^{a,*}

^a Key Laboratory for Colloid and Interface Chemistry of State Education Ministry, School of Chemistry and Chemical Engineering, Shandong University, Jinan, 250100, China

^b College of Chemistry, Chemical Engineering and Material Science, Shandong Normal University, Jinan, 250014, China



ARTICLE INFO

Keywords:
SnO₂ nanocrystal
N-doped graphene
Electrocatalyst
Carbon dioxide electroreduction

ABSTRACT

The electroreduction of carbon dioxide (CO₂) into fuels and other chemicals is an exciting approach to address the urgent climate and energy challenges. However, the unsatisfied efficiency and selectivity for CO₂ reduction reaction (CO₂RR) with conventional electrocatalysts are the major obstacles. Herein, a facile and effective method is developed to deposit ultrasmall SnO₂ nanocrystals on nitrogen-doped graphene via in-situ conversion strategies for highly efficient CO₂RR. The comparison studies reveal that the electrocatalytic activity of such electrocatalysts relies on the loading of SnO₂ on graphene and the nitrogen doping. The optimal electrocatalyst exhibits a high selectivity for CO₂ electroreduction to formate and carbon monoxide at low overpotential (~0.6 V) with a faradaic efficiency of ~ 89% and a current density of ~ 21.3 mA/cm². Additionally, the optimal electrocatalyst shows an excellent stability for 20 h. The good performance would be contributed to the ensemble effect between the highly dispersed ultrasmall SnO₂ nanocrystals and the nitrogen doping on graphene sheets. This work thus provides a rational design strategy for developing efficient CO₂ reduction catalysts.

1. Introduction

The consumption of unsustainable fossil fuels accompanied with excessive release of carbon dioxide (CO₂) into atmosphere has resulted in detrimental environmental issues, such as global warming [1]. To address these issues, electrocatalytic reduction of CO₂ into useful fuels or chemicals (e.g., hydrocarbons, formate) is a promising and environmental benign route for the sustainable energy cycle. However, CO₂ reduction reaction (CO₂RR) is still highly challenging due to the large energy barrier for activating stable CO₂ molecules and the highly competitive hydrogen evolution reaction (HER) in the similar potential range. Therefore, the present effort is devoted to improve the conversion efficiency and selectivity for the electrocatalytic CO₂RR.

In comparison with the noble metal-based electrocatalysts, the naturally abundant metals (e.g., Sn, Cu) have been explored as potential CO₂RR catalysts. Meanwhile, Sn and its oxides are promising candidates due to their highly selectivity for CO₂ reduction into formate and carbon monoxide (CO) [2,3]. Formate as an important intermediate in chemical synthesis has been widely utilized in livestock feed, hydrogen storage, and fuel cell [4–6]. CO can also be converted into valuable liquid fuels or other useful chemicals via the Fischer–Tropsch process [7]. To address the shortages (such as poor stability and conductivity)

of non-noble metal oxides, metal oxides (e.g., SnO₂) have been deposited on carbon materials as electrocatalysts for CO₂RR [8–10]. With the heteroatom doping, the electrocatalytic activities of carbon-based materials for oxygen reduction reaction (ORR), and HER recently have been enhanced due to the charge delocalization mechanism [11,12]. However, the reaction process of CO₂RR is entirely different with those of ORR and HER. Furthermore, the roles of heteroatoms for CO₂RR are quite different in the doped carbon catalysts with various metals or their oxides deposited on. For example, the presence of nitrogen only help the transformation of Co₃O₄ into CoO (the true active phase) in the nanohybrids of Co₃O₄ and nitrogen-doped graphene for CO₂RR [13]. However, Li et.al reported that the pyridinic nitrogen with good adsorption ability for CO₂ and would facilitate the hydrogenation and carbon–carbon coupling reactions on Cu surface for generating C₂H₄ [14]. Varela et al. reported the doped nitrogen atoms are the active sites for CO production whereas Cu centers act as active sites for hydrocarbon formation during CO₂RR [15]. Therefore, it is essential to understand the contributions of heteroatom doping and metal or metal oxides on the electrocatalytic activity of composite catalysts for CO₂RR. Especially, the rational design of a suitable electrocatalysts that can improve the selectivity of CO₂RR in comparison with the competitive hydrogen evolution is highly desirable. The composites of SnO₂ and

* Corresponding author.

E-mail address: jtzhang@sdu.edu.cn (J. Zhang).

graphene have been extensively employed as anode materials for Li-ion batteries, and photocatalytic degradation. However, the hybrid catalyst of SnO₂ and heteroatom doped graphene used for CO₂RR is rarely investigated.

Herein, we demonstrate that the deposition of ultrasmall SnO₂ nanocrystals on reduced graphene oxide (SnO₂/rGO) sheets via the in-situ redox reactions and interfacial hydrolysis. The subsequent annealing of SnO₂/rGO under NH₃ not only provides simple way to introduce nitrogen doping, but also is efficient to prevent the ultrasmall SnO₂ nanocrystals from aggregation. When used as electrocatalysts, the SnO₂ nanocrystals and nitrogen doped graphene exhibit an ensemble effect on CO₂RR to improve the conversion efficiency and selectivity.

2. Methods and experimental section

2.1. Materials

Tin (II) chloride dihydrate (SnCl₂·2H₂O, 98%), dimethyl sulfoxide (DMSO, 99.99%) and HCl (37 wt%) were purchased from Sigma-Aldrich. NaHCO₃ and HCOONa·2H₂O were purchased from Sinopharm Chemical Reagent Co. Ltd. Ultrapure nitrogen, air and carbon dioxide were purchased from Jinan Deyang Gas Co. Ltd. Toray carbon paper (TGP-H-060) was purchased Toray Industries Inc. Nafion 117 membranes (0.180 mm thick, ≥ 0.90 meq/g exchange capacity) were purchased from Alfa Aesar China Co. Ltd. All the regents were used without further purification.

2.2. Materials preparation

Graphene oxide (GO) was synthesized from natural graphite using a modified Hummers method [16]. The deposition of tin oxide (SnO₂) nanoparticles on reduced graphene oxide (rGO) sheets was achieved by the redox reaction between GO and tin (II) ions along with the in-situ hydrolysis. Typically, 5 mL of GO dispersion (4.5 mg mL⁻¹) was diluted into 50 mL of deionized water. 0.14 g of tin (II) chloride dihydrate (SnCl₂·2H₂O) was added to 50 mL of HCl solution (including 1 mL 37 wt % HCl). The above two solutions were mixed and sonicated for 5 min. The mixture was magnetically stirred at 80 °C for 6 h. The obtained precipitate was collected by precipitation naturally, washed with deionized water for several times, and dried by the freeze drying. The obtained sample was named as SnO₂/rGO. The loading of SnO₂ was controlled by adding different amount of SnCl₂·2H₂O (0.07, 0.14, and 0.21 g). The dried product was transferred in a tube furnace and heated to 500 °C with the heating rate of 5 °C/min in the presence NH₃. The obtained samples were labeled as SnO₂/x@N-rGO (x presents the amounts of SnCl₂·2H₂O). For comparison, the SnO₂/0.14@rGO was synthesized by the same produce using N₂ instead of NH₃ in the thermal treatment. rGO aerogel was also prepared by using the same procedure in the absence of Sn²⁺ ions. The subsequent annealing in NH₃ atmosphere results in the formation of nitrogen doped rGO (N-rGO). For comparison, the samples were also synthesized at 500 °C by adjusting the ratio between NH₃ and N₂ in the annealing gas. The obtained samples were defined as SnO₂/0.14@N-rGO-1 and SnO₂/0.14@N-rGO-2.

2.3. Materials characterization

X-ray diffraction (XRD) was performed by using a Rigaku Dmax-rc X-ray diffractometer with Ni-filtered Cu K α ($\lambda = 1.5418 \text{ \AA}$) radiation. High-resolution transmission electron microscopy (HRTEM) was carried out on a JEM-2100 F. Scanning electron microscopy (SEM) was conducted on a Hitachi SU-70 FESEM. X-ray photoelectron spectroscopy (XPS) was performed with a photoelectron spectrometer (ESCALAB 250). N₂ adsorption-desorption isotherms and CO₂ adsorption were measured on a Quantachrome instruments. Atomic force microscopy (AFM) was performed by means of Veeco DI Nano-scope

MultiMode V system. FTIR spectra were tested on Nicolet 6700 Fourier transform infrared spectrometer.

2.4. Electrochemical characterization

Electrochemical measurements were implemented on an electrochemical workstation (CHI model 760E) with a typical H-type cell (Figure S1). To prepare the working electrode, 10 mg of the samples were firstly dispersed in 2 ml aqueous solution including 0.14 mL of 5 wt% Nafion solution under sonication. The obtained homogeneous catalyst ink was then dropped onto a Toray carbon paper (1 × 1 cm) and dried at room temperature. The mass loading was 0.3 mg cm⁻² unless otherwise noted. An Ag/AgCl electrode and a piece of Pt plate were used as the reference and counter electrodes, respectively. A Nafion 117 proton exchange membrane was used to separate the working and counter electrodes. For CO₂ reduction, linear sweep voltammetry (LSV) measurement with a scan rate of 20 mV s⁻¹ in the potential range of -0.5 to -1.2 V vs. RHE was carried out in CO₂ (or N₂)-saturated 0.5 M NaHCO₃ solution (pH = 7.2). The electrolyte was purged with CO₂ or N₂ for 30 min prior to the measurement. CO₂ was humidified with water by passing through a bubbler to minimize the evaporation of electrolyte. The cathodic compartment was stirred to enhance the mass transport of CO₂ in the electrolyte. The obtained data were calibrated with respect to the reversible hydrogen electrode (RHE) by $E_{(\text{vs. RHE})} = E_{(\text{vs. Ag/AgCl})} + 0.21 \text{ V} + 0.0591 \times \text{pH}$. The electrochemical impedance spectroscopy (EIS) was performed with Gamry potentiostat. The stability test of SnO₂/0.14@N-rGO catalyst was performed at -0.8 V vs. RHE for 20 h with the CO₂ flow rate of 3 mL min⁻¹, and the flow rate was regulated by a mass flow controller during electrolysis.

2.5. Product analysis

The gas products of CO₂ electrocatalytic reduction were monitored by a gas chromatography (GC) (GC7290) equipped with a thermal conductivity detector (TCD) detector and Molsieve 5 A column. The hydrogen (H₂) gas was detected and analyzed by a TCD. The CO gas was quantified by a flame ionization detector (FID). The concentrations of H₂ and CO were calculated by the corresponding standard curves, respectively. The electrolyte after reaction was collected and analyzed on a Varian 400 MHz NMR spectrometer to quantify liquid products. 0.5 mL of the electrolyte was mixed with 0.1 mL D₂O and 0.1 mL 6 mM DMSO was added as an internal standard. The 1D ¹H spectrum was measured with water suppression. The standard curve was made by using different concentrations of sodium formate and a certain amount of the internal standard (DMSO), [17] as shown in Figure S2. The area ratio of the formate peak to the DMSO peak was plotted in the standard curve to quantify the concentration of formate. Faradaic efficiency (FE) for a specific product (CO, formate, H₂) is calculated using the Eq. (1) [18]:

$$\varepsilon_{\text{Faradaic}} = \frac{\alpha nF}{Q} \quad (1)$$

in which α is the number of electrons transferred (e.g., $\alpha = 2$ for reduction of CO₂ to CO, formate, H₂). n refers to the number of moles for a desired product. F is Faraday's constant. Q is the charge passed for one hour reaction.

2.6. Average particle size, Electrochemical active surface area, and Turnover frequency

The average particle size of SnO₂ nanocrystals can be calculated by using the scherrer equation [19]:

$$D = \frac{K\lambda_{K\alpha 1}}{B_{2\theta} \cos \theta_{\max}} \quad (2)$$

in which D is the mean particle size, $\lambda_{\text{K}\alpha 1}$ is the X-ray wavelength ($\lambda = 1.5418 \text{ \AA}$), θ_{\max} is the angle for the (110) plane, and $B_{2\theta}$ is the band width at the half height for the SnO_2 (110) plane.

The electrochemical active surface area (ECSA) of an electrocatalyst is estimated from the electrochemical double-layer capacitance (C_{dl}). The C_{dl} was determined by measuring the CV curves at different scan rates (0.01, 0.02, 0.04, 0.06, 0.08, 0.1, and 0.12 V S^{-1}) in the non-Faradaic potential range. Δj is the current difference between anodic (j_a) and cathodic current density (j_c) at the midpoint of applied potential window (0.625 V vs. RHE). The ECSA of a catalyst sample is calculated from the double layer capacitance according to Eq. (3) [20]:

$$\text{ECSA} = \frac{C_{dl}}{C_s} \quad (3)$$

where C_s ($22 \mu\text{F cm}^{-2}$) is the specific capacitance of the sample or the capacitance of an atomically smooth planar surface of the material per unit area under identical electrolyte conditions.

The turn over frequency (TOF) of active sites for CO_2 reduction into formate on $\text{SnO}_2/0.14@\text{N-rGO}$ and $\text{SnO}_2/0.14@\text{rGO}$ was calculated at different over-potentials according to the Eq. (4) [21]:

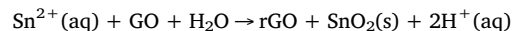
$$\text{TOF}(\text{s}^{-1}) = \frac{\text{The rate of product formation}}{\text{The number of } \text{SnO}_2 \text{ atoms} + \text{the mnmbnr of nitrogen atoms}} \\ = \frac{i_0 (\text{A} \cdot \text{cm}^{-2}) \times FE}{\text{active sites density} \times e \times n} \quad (4)$$

where e refers to the elementary charge ($1.602 \times 10^{-19} \text{ C}$), n refers to the number of electrons transferred to generate the special product ($n = 2$ for formate). On the basis of the ensemble effect of SnO_2 and nitrogen doping, SnO_2 and doped nitrogen are the active sites for CO_2RR , we hypothesis the all sites should be electrochemically accessible. Therefore, the active sites density (site/cm^2) can be calculated by XPS results and the mass loading of the working electrode. For $\text{SnO}_2/0.14@\text{rGO}$ without nitrogen doping, the number of nitrogen is zero.

3. Results and discussion

3.1. Description of the catalysts formation process

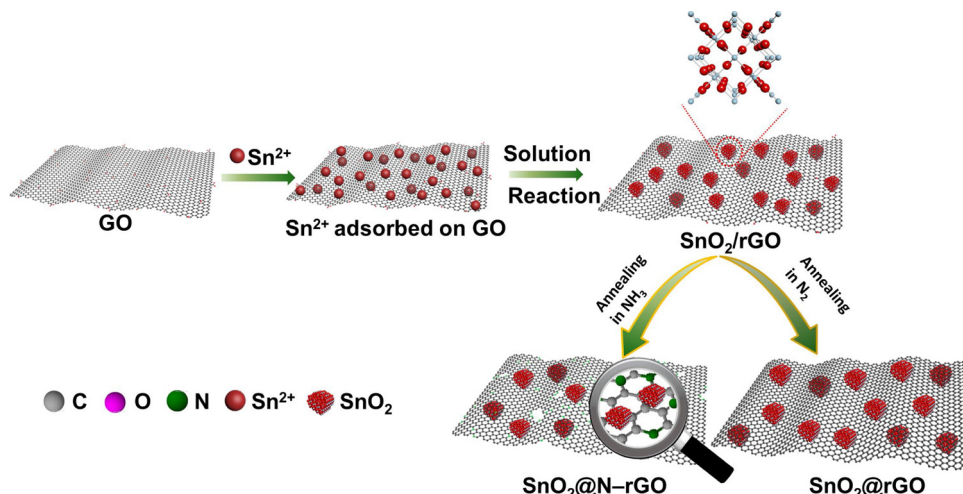
As illustrated in Scheme 1, two steps were involved for the preparation of $\text{SnO}_2@\text{N-rGO}$ and $\text{SnO}_2@\text{rGO}$ nanocomposites. Firstly, Sn^{2+} ions would be adsorbed on the GO surface via electrostatic interactions due to the ionization of oxygenate functional groups (such as carboxyl, hydroxyl, and epoxy). Sn^{2+} ions are able to reduce GO sheets and at the same time the interfacial hydrolysis of metal ions leads to the in-situ deposition of SnO_2 nanoparticles on the rGO surface: [22,23]



The successful synthesis of SnO_2/rGO composites with various ratios can be proved by the X-ray diffraction (XRD) patterns and transmission electron microscopy (TEM) (Figure S3). The typical XRD peaks in Figure S3a would be ascribed to the diffraction features of tetragonal rutile phase SnO_2 (JCPDS 41–1445). The TEM images (Figures S3b and S3d) clearly show that lots of SnO_2 nanoparticles are dispersed on rGO sheets. During the redox reaction, residual oxygen containing functional groups (e.g., carboxyl groups) would be left on rGO nanosheets due to the weak reducing ability of Sn^{2+} ions. Therefore, the ultrasmall SnO_2 nanoparticles would interact with the graphene sheets through hydrogen bonding, electrostatic binding or charge transfer interactions. [24,25] Such similar interactions were also reported among other metal (hydro)oxides and rGO systems, such as $\text{Ni(OH)}_2/\text{rGO}$ via chemisorption and van der Waals interactions, [26] ZIF-67 and rGO via the electrostatic attraction [27,28]. Therefore, the interaction between SnO_2 nanoparticles and rGO nanosheets enables the uniform deposition of ultrasmall SnO_2 nanoparticles on rGO sheets. Furthermore, the number of SnO_2 nanoparticles deposited on the surface increases with the increasing ratio of Sn^{2+}/GO (e.g., $\text{SnO}_2/0.07/\text{rGO}$, $\text{SnO}_2/0.14/\text{rGO}$ and $\text{SnO}_2/0.21/\text{rGO}$). Subsequently, the high crystalline $\text{SnO}_2@\text{N-rGO}$ nanocomposites were prepared via the annealing treatment in NH_3 during which NH_3 provides the nitrogen source for forming nitrogen doping. For comparison, the sample was also annealed in N_2 atmosphere to prepare $\text{SnO}_2@\text{rGO}$ (Scheme 1).

3.2. Microstructure and composition characterization of electrocatalysts

The scanning electron microscopy (SEM) image (Fig. 1a) exhibits two-dimensional rGO sheets with many wrinkles, on which lots of SnO_2 nanoparticles are uniformly dispersed. TEM images (Fig. 1b, c) exhibit the nearly transparency rGO sheets are covered with lots of black dots ascribed to the SnO_2 nanoparticles, which is in good agreement with SEM results. The enlarged TEM image (Fig. 1d) reveals that the lattice spacing of $\sim 0.33 \text{ nm}$ is corresponding to the (110) planes of SnO_2 . The TEM image and the corresponding energy dispersive X-ray spectroscopy (EDS) mapping image (Fig. 1e, f) show the uniform distribution of C, N, O, Sn elements, suggesting the formation of SnO_2 and nitrogen doped rGO ($\text{SnO}_2@\text{N-rGO}$). The presence of SnO_2 nanoparticles would prevent the restacking of graphene sheets after the removal of oxygenate functional groups, thereby increasing the stability of individual graphene sheets. The AFM image (Fig. 1g) demonstrates the lateral dimension of the $\text{SnO}_2/0.14@\text{N-rGO}$ sheet is in the micrometer scales, and the uniform layer structure with a thickness of $\sim 4.2 \text{ nm}$ (Fig. 1h) suggests the ultrathin layer nature.



Scheme 1. Schematic illustration for the preparation of $\text{SnO}_2@\text{N-rGO}$ and $\text{SnO}_2@\text{rGO}$ nanocomposites, respectively.

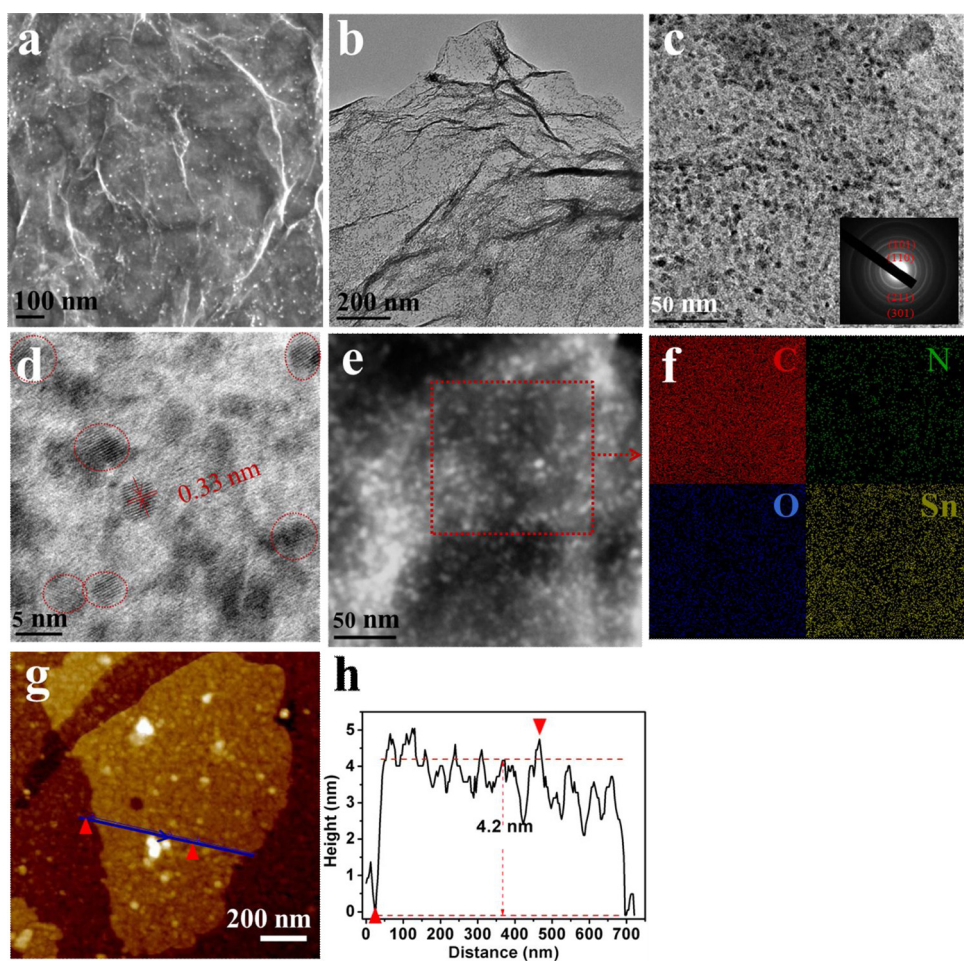


Fig. 1. (a) SEM image of $\text{SnO}_2/0.14@\text{N-rGO}$. (b–d) TEM and HRTEM images of $\text{SnO}_2/0.14@\text{N-rGO}$. TEM image (e) and the corresponding elemental mapping images (f) of $\text{SnO}_2/0.14@\text{N-rGO}$. (g, h) AFM image and corresponding height profiles of $\text{SnO}_2/0.14@\text{N-rGO}$.

The TEM images (Figure S4) of composites with various SnO_2 loadings exhibit that the number of SnO_2 nanoparticles increases with increasing the mass loading. However, the particle size distribution curves reveal that the average particle size is 3.6 ± 0.4 , 3.9 ± 0.3 , and 4.1 ± 0.6 nm for $\text{SnO}_2/0.07@\text{N-rGO}$, $\text{SnO}_2/0.14@\text{N-rGO}$, and $\text{SnO}_2/0.21@\text{N-rGO}$, respectively (Figure S5). The results indicate the samples annealed in NH_3 exhibit the similar particle size of $\sim 3\text{--}4$ nm (Figures S4a & 4c). In contrast, the $\text{SnO}_2/0.14@\text{rGO}$ sample annealed in the presence of N_2 exhibits the obviously larger particle size of ~ 7 nm (Figure S5d). Furthermore, the SnO_2 nanoparticles aggregate together on the rGO sheets (Figure S4e and S4f). As discussed above, the oxygenate groups of rGO would facilitate the in-situ deposition of SnO_2 nanoparticles. However, rGO sheets would be further reduced due to the deoxygenated process under thermal treatment [29]. The removal of residual oxygenate functional groups on which SnO_2 are prefer to anchor, would result in the aggregation of SnO_2 clusters with larger particle size (Figures S4e & 4f). When annealed in NH_3 atmosphere, nitrogen atoms are doped into rGO sheets along with the deoxygenated process, which would provide the new active sites for anchoring SnO_2 nanoparticles [13,30]. Therefore, SnO_2 nanoparticles with similar size remains uniformly dispersed on the surface of N-rGO sheets.

The XRD patterns (Fig. 2a) exhibit that the sharp diffraction peak at about $2\theta = 10.4^\circ$ would be ascribed to the (002) reflection of stacked GO sheets with an interlayer spacing of ~ 0.86 nm. The larger interlayer distance in comparison with pristine graphite (0.34 nm) suggests the introduction of various oxygen-containing groups (e.g., carboxyl, hydroxyl, or epoxy) on GO sheets [31]. After the deposition of SnO_2 nanoparticles and thermal treatment, the XRD peaks can be indexed to

the typical diffractions of SnO_2 , suggesting the formation of pure tetragonal SnO_2 crystals. Additionally, the thermal treatment would enhance the crystallinity of SnO_2 nanoparticles in comparison with the weak diffraction peaks of as-prepared samples (Figure S5a). No obvious peak at $\sim 26^\circ$ related to rGO is observed. Thus, the restacking of rGO sheets would be prevented due to the presence of SnO_2 nanoparticles [9,10]. The mean crystallite sizes of SnO_2 nanoparticles for $\text{SnO}_2/0.07@\text{N-rGO}$, $\text{SnO}_2/0.14@\text{N-rGO}$, $\text{SnO}_2/0.21@\text{N-rGO}$ and $\text{SnO}_2/0.14@\text{rGO}$ are 3.65, 3.72, 3.93, and 6.37 nm, respectively according to the scherer equation, which is consistent with the particle size distribution in the TEM images. These high crystalline composites with better conductivity as electrocatalysts are beneficial to further improve the catalytic performance [32].

The FTIR spectrum (Fig. 2b) of GO exhibits that the absorption peaks at 1723, 1380, 1061, 1220 and 1615 cm^{-1} can be ascribed to COOH, $-\text{OH}$, epoxy C–O stretching vibrations, C–OH stretching, and C–C aromatic ring modes, respectively. The peak at around 827 cm^{-1} (weak) could be assigned to O=C=O. [33] In comparison with GO, the peaks for oxygenate functional groups are obviously suppressed whereas new peaks are observed at about 600 cm^{-1} , which are ascribed to the oxygen vibration in tin oxides ($\text{Sn}-\text{O}$). [34] The FTIR results confirmed the oxidation and hydrolysis of Sn^{2+} ions into SnO_2 nanocrystals on rGO surface. The Raman spectra of as-prepared samples are shown in Fig. 2c. The two peaks at ~ 1331 and 1591 cm^{-1} are corresponding to the in-plane vibrations of the defective (D) and graphitic (G) carbons, respectively. Generally, the intensity ratio of D/G band (I_D/I_G) can estimate approximately the degree of disorder in the graphitic carbon materials. The I_D/I_G ratios of samples (1.48, 1.52, and

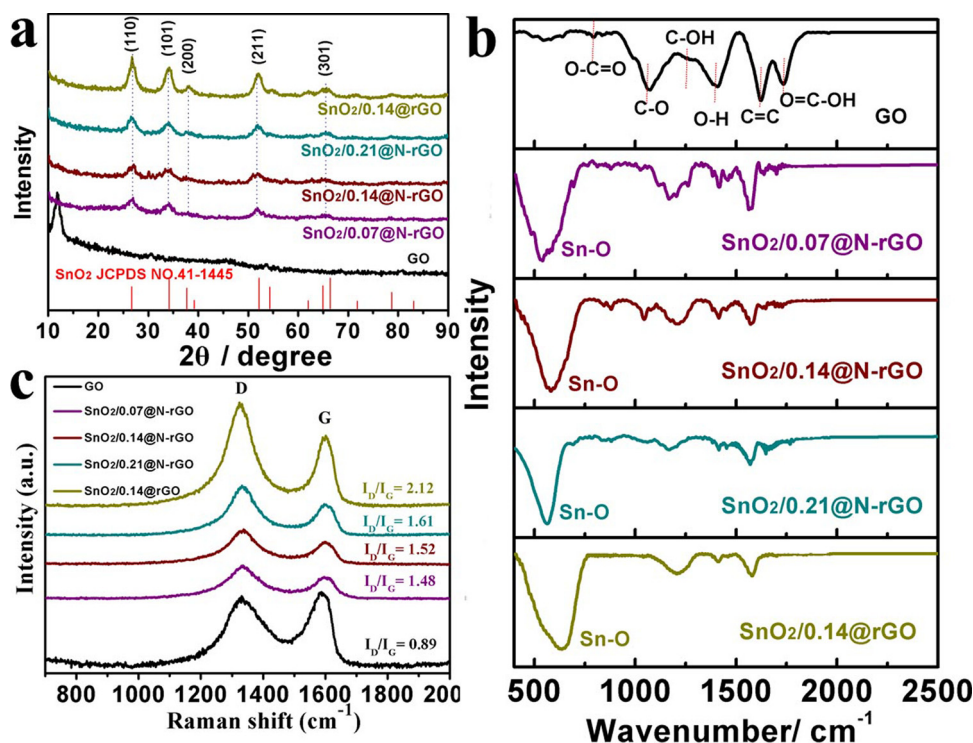


Fig. 2. The XRD (a), IR (b) and Raman (c) of as-prepared samples GO, SnO₂/0.07@N-rGO, SnO₂/0.14@N-rGO, SnO₂/0.21@N-rGO, and SnO₂/0.14@rGO.

1.61 for SnO₂/0.07@N-rGO, SnO₂/0.14@N-rGO, and SnO₂/0.21@N-rGO, respectively) are larger than that of GO (0.89). The higher I_D/I_G ratio of SnO₂@N-rGO composites would be contributed to the additional defects due to the nitrogen doping [13,23].

The survey XPS spectra reveal the presence of C, N, O, and Sn elements for SnO₂/0.14@N-rGO (Fig. 3a) and C, O, and Sn elements for SnO₂/0.14@rGO (Figure S6 and Table S1). The Sn 3d_{5/2} (487.3 eV) and 3d_{3/2} (495.8 eV) (Fig. 3b and S6b) suggest that the oxidation state of Sn

in the nanoparticles is Sn(IV), exhibiting the formation of SnO₂ [35]. For C 1 s, the C–N bond (285.6 eV) confirms the formation of nitrogen-doping (Fig. 3c). [31] The core-level O 1 s spectra of SnO₂/0.14@N-rGO (Fig. 3d) and SnO₂/0.14@rGO (Figure S6c) with asymmetric shapes can be divided into two peaks at 531.7 (Sn-O-C) and 532.9 eV (C–O–C) [36]. Additionally, the high-resolution N 1 s spectrum of SnO₂/0.14@N-rGO has been divided into four peaks corresponding to the pyridinic N (398.4 eV), pyrrolic N (399.8 eV), graphitic

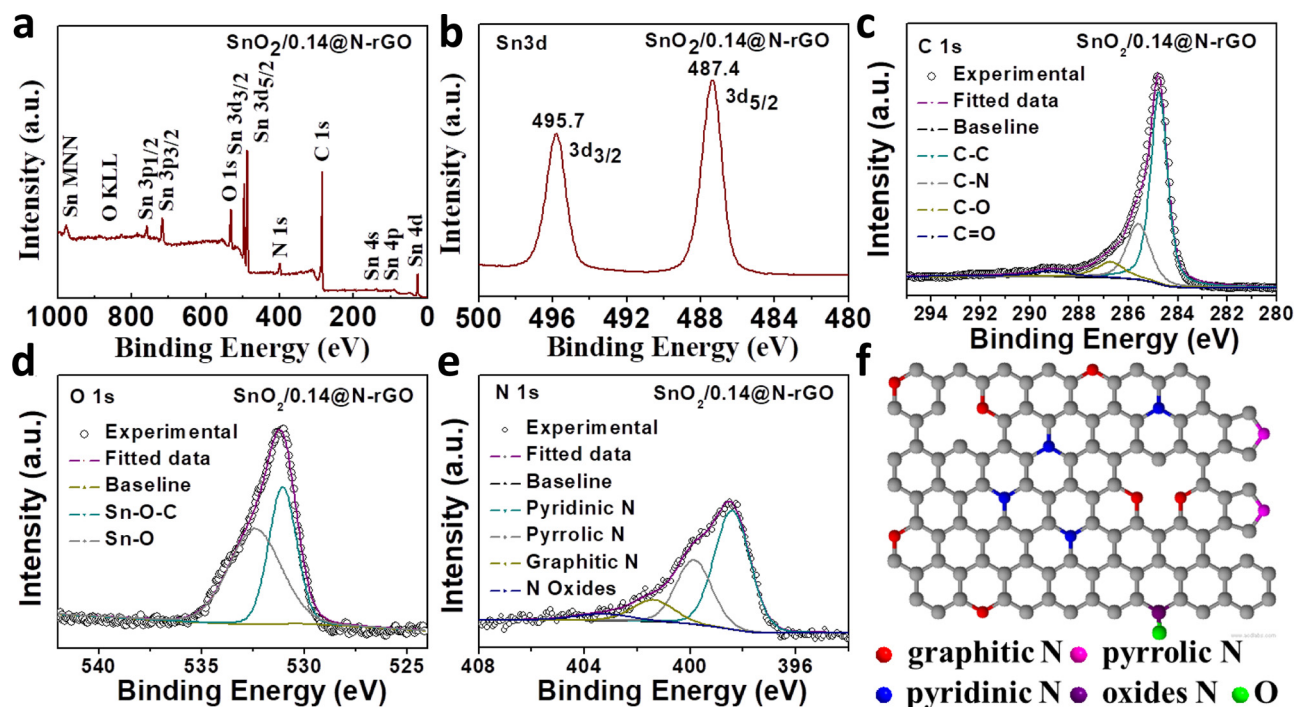


Fig. 3. (a) XPS survey spectra of SnO₂/0.14@N-rGO. High-resolution XPS spectra of (b) Sn 3d, (c) C 1s, (d) O 1s, (e) N 1s. (f) Schematic of pyridinic, graphitic, pyrrolic and oxides N configuration in N doped graphene.

N (401.4 eV) and oxidized pyridinic N (403.3 eV) (Fig. 3e) [37]. Moreover, the pyridinic N has the highest relative ratio (3.48 atom%) than those of the pyrrolic N (1.90 atom%), graphitic N (0.76 atom%) and oxidized pyridinic N (0.31 atom%). According to the previous reports, pyridinic nitrogen is expected to act as anchoring sites for the growth of SnO_2 due to their coordination capabilities [13,30]. Table S1 shows the surface composition of the $\text{SnO}_2/0.14@\text{N-rGO}$ and $\text{SnO}_2/0.14@\text{rGO}$ samples determined from XPS. According to the XPS results, the formation of hybrid materials of SnO_2 nanoparticles and the nitrogen doped graphene can be achieved by simple annealing in NH_3 .

N_2 adsorption–desorption isotherms and the pore size distribution curves (Figure S7) reveal the mesoporous structure of composite samples [25]. More importantly, the specific surface area for $\text{SnO}_2/0.07@\text{N-rGO}$, $\text{SnO}_2/0.14@\text{N-rGO}$, $\text{SnO}_2/0.21@\text{N-rGO}$ and $\text{SnO}_2/0.14@\text{rGO}$ was calculated to be 168.6, 224.7, 272.1 and 205.6 $\text{m}^2 \text{g}^{-1}$, much larger than those reported results previously [33,38]. The decoration of both sides of N-rGO with SnO_2 nanoparticles is efficient to prevent the aggregation of rGO sheets, leading to the enhanced specific surface area. The $\text{SnO}_2/0.14@\text{N-rGO}$ sample with the largest surface area and mesoporous structure will be advantageous to the rapid mass transport and electron transfer for improving electrocatalytic activity.

3.3. Electrocatalytic performance of the catalysts

The electrocatalytic activities of $\text{SnO}_2@\text{N-rGO}$ samples toward CO_2RR were investigated by linear sweep voltammetry (LSV). In addition to the reduction peak of SnO_2 nanoparticles at $\sim -0.22 \text{ V}$, [2,39] the abrupt current increase from $\sim -0.5 \text{ V}$ (Fig. 4a) would be ascribed to the electrocatalytic reduction of CO_2 in the CO_2 -saturated electrolyte. However, $\text{SnO}_2/0.14@\text{rGO}$ and N-rGO (Figure S8) exhibit almost the similar current curves at the same potential, indicating their poor electrocatalytic activities for CO_2RR . Notably, the current densities of the $\text{SnO}_2/0.07@\text{N-rGO}$, $\text{SnO}_2/0.14@\text{N-rGO}$, and $\text{SnO}_2/0.21@\text{N-rGO}$ samples are much larger than those of the previous reported catalysts, [39] suggesting the high efficiency for CO_2RR in the same potential. More importantly, the $\text{SnO}_2/0.14@\text{N-rGO}$ electrode displays the highest current density of 50 mA cm^{-2} at -1.0 V vs. RHE among the three $\text{SnO}_2@\text{N-rGO}$ catalysts. Moreover, the onset potential of the $\text{SnO}_2/0.14@\text{N-rGO}$ (-0.48 V vs. RHE) is more positive than others. However, a further increment in the loading of SnO_2 ($\text{SnO}_2/0.21@\text{N-rGO}$) has a negative effect on the electrochemical activity, exhibiting lower current density. The better performance would be attributed to the ensemble effect of the well-dispersed SnO_2 nanoparticles with larger number of active centers and the N-rGO sheets with high surface area and good conductivity.

To examine and quantify products for CO_2 electroreduction, the $\text{SnO}_2/0.07@\text{N-rGO}$, $\text{SnO}_2/0.14@\text{N-rGO}$, $\text{SnO}_2/0.21@\text{N-rGO}$ and $\text{SnO}_2/0.14@\text{rGO}$ as electrocatalysts were performed at a series of constant potential electrolysis in a gas-tight H-cell with CO_2 -saturated electrolyte. The plots of current density against potentials (Fig. 4b) exhibit that the kinetics of reduction reactions have been linearly boosted up as the applied electrode potential negatively shifted beyond -0.6 V vs. RHE. As revealed in Fig. 4c-f, formate, CO, and H_2 are the main products with a combined faradaic efficiency (FE) of $\sim 100\%$ over the whole potential range. Additionally, the control experiment (Figure S9) exhibits no formate is detected by NMR and no CO is detected by GC in N_2 -saturated 0.5 M NaHCO_3 electrolyte at -0.8 V vs. RHE for 1 h, suggesting carbon dioxide is the direct carbon source for producing formate and CO. The selectivity towards formate and H_2 is strongly dependent on the applied potential, whereas FE for CO (less than about 12%) does not vary significantly (Fig. 4c and f). At an applied potential of -0.5 V , formate with a FE of about 13.5, 24, 15, and 5% for $\text{SnO}_2/0.07@\text{N-rGO}$, $\text{SnO}_2/0.14@\text{N-rGO}$, $\text{SnO}_2/0.21@\text{N-rGO}$ and $\text{SnO}_2/0.14@\text{rGO}$, respectively, was detected. However, H_2 is the dominant product at this potential. With increasing overpotential, the FE for formate firstly increases and then decreases rapidly. The FE for

formate reaches to the maximal value of 42, 78, 51.2 and 26% for $\text{SnO}_2/0.07@\text{N-rGO}$, $\text{SnO}_2/0.14@\text{N-rGO}$, $\text{SnO}_2/0.21@\text{N-rGO}$ and $\text{SnO}_2/0.14@\text{rGO}$ at -0.8 V , respectively. This potential to achieve the highest formate selectivity is more positive in comparison to the previous reports (-1.0 V vs. RHE) and the current density is much higher than those of the most previous reports. (Table S3) [13,38]. The FE for H_2 shows an opposite trend at the potential range. At the low overpotentials, the thermodynamically and kinetically favorable HER is dominant [38]. With increasing overpotential, the kinetics of both CO_2 reduction and HER are improved. However, at the higher overpotential, FE of HER is higher than that of CO_2 reduction due to the mass-transport process limited by the low concentration of CO_2 in the aqueous electrolyte. Notably, the above four samples achieved the maximal FE for formate generation at the similar potentials, which could be ascribed to the mass transport limitation of CO_2 and the competitive HER [37]. However, the $\text{SnO}_2/0.14@\text{rGO}$ electrode exhibits the lowest activity for CO_2RR to formate, with the dominant product of H_2 in the applied potentials (Fig. 4f). Specially, no product for CO_2RR is observed on the rGO electrode. These results indicate that SnO_2 nanoparticles and nitrogen doping on graphene play ensemble roles in enhancing the electrocatalytic reduction of CO_2 to formate.

For the formation of formate (Fig. 5a), it has been proposed that the adsorbed CO_2 ($\text{CO}_{2\text{ads}}$) is initially converted to $\text{CO}_2\cdot^-$ with an one electron (e^-) transfer, and the subsequent chemical reaction with the H^+ transfer step enables the formation of intermediate (HCOO^*). Then, incorporated with the second electron, the adsorbed HCOO^- ($\text{HCOO}_{\text{ads}}^-$) forms and tends to directly break away from the electrode surface into solution. [38,39] To evaluate the kinetics of the electrocatalytic reaction, the Tafel plots derived from constant potential electrolysis are 157, 133, 154, and 116 mV dec^{-1} for $\text{SnO}_2/0.07@\text{N-rGO}$, $\text{SnO}_2/0.14@\text{N-rGO}$, $\text{SnO}_2/0.21@\text{N-rGO}$, and $\text{SnO}_2/0.14@\text{rGO}$, close to 118 mV dec^{-1} (Fig. 5b and S10). The results suggest that the formation rate of formate would be limited by the first single electron transfer step in the present case. Thus, the formation of $\text{CO}_2\cdot^-$ intermediate is presumably the rate-determining step.

With regard to the notable enhancement of catalytic activity for $\text{SnO}_2/0.14@\text{N-rGO}$, the increase in electrochemical active surface area (ECSA) may be one of the important contributors since larger ECSA could afford more catalytically active sites. According to the measured double-layer capacitance, the ECSA of $\text{SnO}_2/0.14@\text{N-rGO}$ (225.5 cm^2) was estimated to be ~ 1.99 , 1.34 and 1.37 times larger than that of $\text{SnO}_2/0.07@\text{N-rGO}$ (112.9 cm^2), $\text{SnO}_2/0.21@\text{N-rGO}$ (163.6 cm^2), and $\text{SnO}_2/0.14@\text{rGO}$ (167.3 cm^2) (Figure S11). The large ECSA of $\text{SnO}_2/0.14@\text{N-rGO}$ indicates the remarkably large amount of active sites for CO_2RR . Table S2 shows the $\text{SnO}_2/0.14@\text{N-rGO}$ have the highest values of C_{dl} , ECSA, and R_f , which further testify the reason of good catalytic performance. Additionally, the CO_2 isotherms exhibit the good CO_2 adsorption capacity of $\text{SnO}_2/0.14@\text{N-rGO}$ (Fig. 5c). Specifically, the amount of CO_2 adsorption capacity for $\text{SnO}_2/0.14@\text{N-rGO}$ could reach 48.1 mg g^{-1} at 1 atm , which is roughly 1.64 times higher than that of $\text{SnO}_2/0.14@\text{rGO}$ (29.3 mg g^{-1}). The admirable CO_2 adsorption capability would be contributed to the porous structure and the nitrogen doping. [40] Furthermore, electrochemical impedance spectroscopy (EIS) (Fig. 5d) reveals that the smallest charge-transfer resistance of $\text{SnO}_2/0.14@\text{N-rGO}$ in comparison with $\text{SnO}_2/0.07@\text{N-rGO}$, $\text{SnO}_2/0.21@\text{N-rGO}$. The presence of highly-conductive rGO could enhance the overall electronic conductivity, thus ensuring the fast electron transfer to CO_2 for forming $\text{CO}_2\cdot^-$ intermediate. Notably, $\text{SnO}_2/0.14@\text{rGO}$ exhibits the lowest charge-transfer resistance. However, the efficient electron transfer would contribute to the HER (Fig. 4f and S8) rather than the formation of $\text{CO}_2\cdot^-$ intermediate due to the weak CO_2 adsorption without nitrogen doping (Fig. 5c). Therefore, the above results strongly demonstrate that the incorporation of SnO_2 nanocrystals with the N-doped graphene would greatly improve the CO_2 reduction performances.

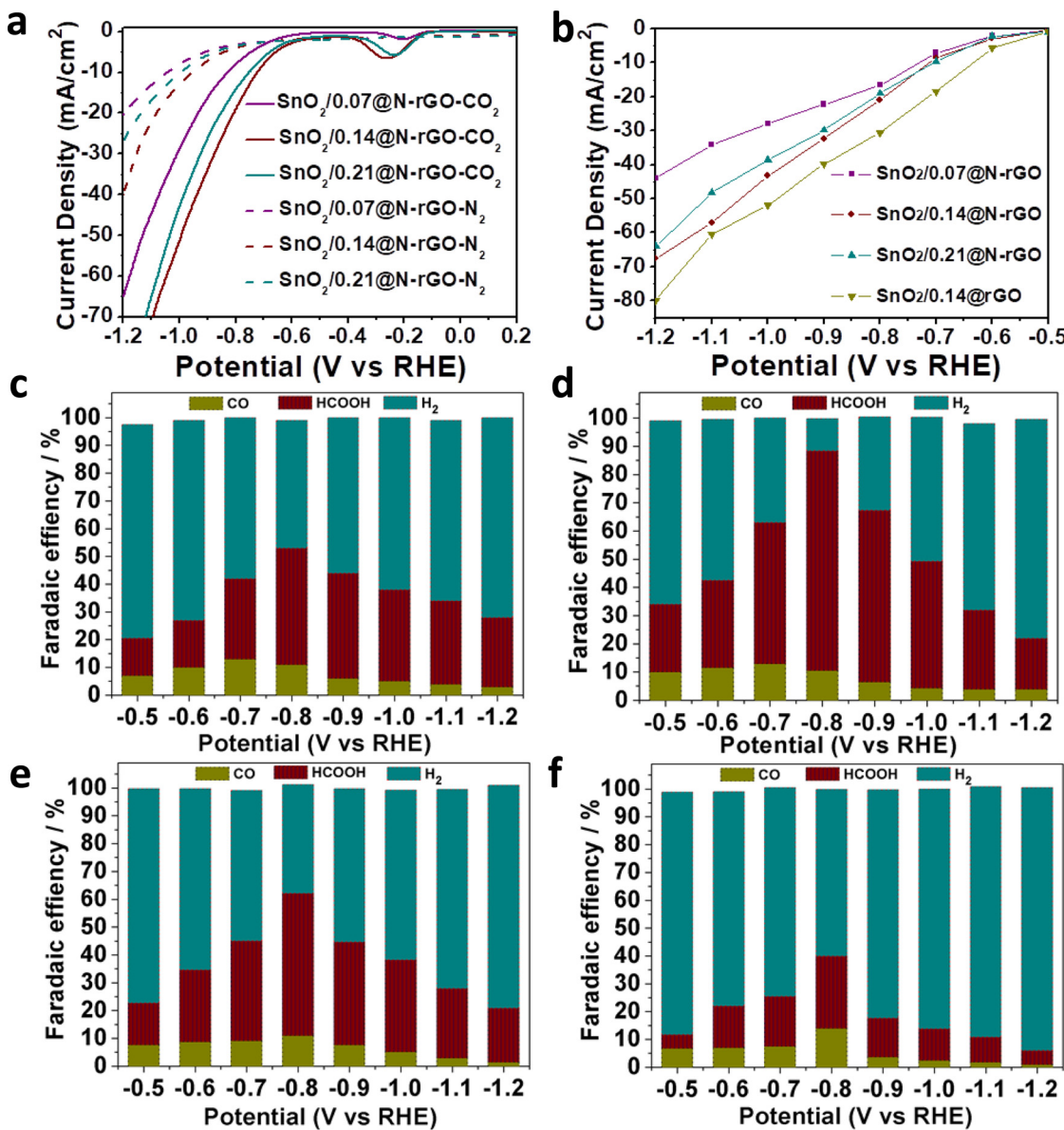


Fig. 4. (a) LSV in N_2 - and CO_2 -saturated 0.5 M NaHCO_3 at a scan rate of 20 mV s^{-1} . (b) Current density in CO_2 -saturated 0.5 M NaHCO_3 solution at different applied potentials. Faradaic efficiency of CO, formate, and H_2 for $\text{SnO}_2/0.07@\text{N-rGO}$ (c), $\text{SnO}_2/0.14@\text{N-rGO}$ (d), $\text{SnO}_2/0.21@\text{N-rGO}$ (e) and $\text{SnO}_2/0.14@\text{rGO}$ (f) electrode at different potentials.

3.4. Ensemble effect of nitrogen doping and ultrasmall SnO_2 nanocrystals on graphene sheet

As discussed above, the high activity and selectivity for formate on $\text{SnO}_2/0.14@\text{N-rGO}$ electrode would be ascribed to the ensemble effect of nitrogen doping and ultrasmall SnO_2 nanocrystals on graphene sheets. The nitrogen doping of the graphene sheets would facilitate the surface adsorption of CO_2 molecules on the graphene surface due to the strong Lewis basicity [40]. The adsorbed CO_2 molecules would subsequently convert into $\text{CO}_2^{\cdot-}$ intermediate via the initial one electron transfer, and the conversion would be enhanced along the highly conductive rGO sheets (Fig. 5a). To determine the effect of nitrogen doping, the samples were also prepared by adjusting the ratio between NH_3 and N_2 in the annealing gas at the same temperature. The obtained samples with nitrogen content of 2.50, 3.24 atom%, respectively exhibits the improved catalytic performance with increasing nitrogen content (Figure S12). However, $\text{SnO}_2/0.14@\text{N-rGO}$ with the highest N content exhibit the best catalytic performance for CO_2RR (Figure S13). The higher N content would facilitate the surface adsorption of CO_2 ,

Subsequently, SnO_2 nanocrystals as the active sites is able to promote the chemical reaction with one proton transfer to generate the intermediate (HCOO^*) via energetically favorable $\text{SnO}_2\text{-O}$ interaction due to the surface rich oxygenate groups [41]. Then, the HCOO_{ads} generated with the rapid transfer of the second electron would be released easily from the electrode surface [42]. It can be seen that the nitrogen doping and SnO_2 nanocrystals on the surface of rGO sheets synergistically favour CO_2 adsorption, conversion, and stabilization of intermediates, leading to the formation of formate. The detailed mechanism is needed to further determine via in-depth understanding of the electrocatalyst and reaction process. Nevertheless, the ensemble effect of $\text{SnO}_2/0.14@\text{N-rGO}$ is favorable to enhance the activity and selectivity for the formate formation.

3.5. Turnover frequency and stability test of electrocatalysts

Turnover frequency (TOF) of formate formation (Fig. 6a) was calculated to demonstrate the per-site activity of catalysts for producing formate. Without nitrogen doping, the TOF of $\text{SnO}_2/0.14@\text{rGO}$ are

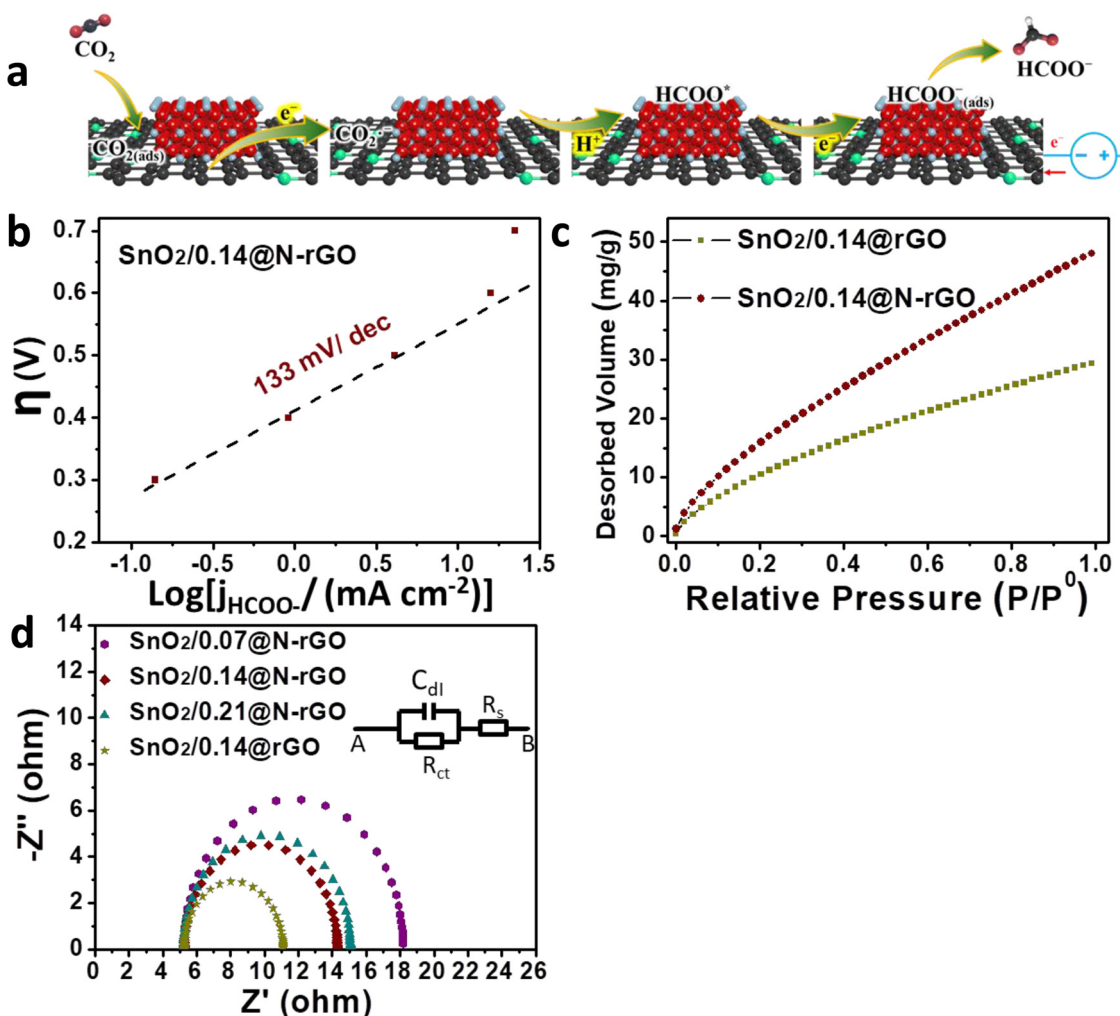


Fig. 5. (a) Proposed electroreduction of CO_2 to formate on the $\text{SnO}_2/\text{N-rGO}$ catalysts. (b) Tafel plot of the $\text{SnO}_2/0.14@\text{N-rGO}$ electrode for producing formate. (c) CO_2 adsorption isotherms of $\text{SnO}_2/0.14@\text{N-rGO}$ and $\text{SnO}_2/0.14@\text{rGO}$. (d) EIS nyquist plots of $\text{SnO}_2/0.07@\text{N-rGO}$, $\text{SnO}_2/0.14@\text{N-rGO}$, $\text{SnO}_2/0.21@\text{N-rGO}$ and $\text{SnO}_2/0.14@\text{rGO}$ electrodes in CO_2 -saturated 0.5 M NaHCO_3 (-0.85 V vs. RHE), and the inset shows the equivalent circuit impedance model.

much lower than those of $\text{SnO}_2/0.14@\text{N-rGO}$ in the overpotential range of 0.5–1.0 V. Typically, the TOF for $\text{SnO}_2/0.14@\text{N-rGO}$ (4.7 s^{-1}) is around two-time larger than that for $\text{SnO}_2/0.14@\text{rGO}$ (2.5 s^{-1}) at the overpotential of 0.6 V, suggesting the high efficiency of $\text{SnO}_2/0.14@\text{N-rGO}$ because of the ensemble effect of nitrogen doping and SnO_2 nanocrystals on graphene sheets. To evaluate the stability of the $\text{SnO}_2/0.14@\text{N-rGO}$ electrode, electrolysis at a fixed potential of -0.8 (vs. RHE) was carried out over an extended period. It can be seen that the

$\text{SnO}_2/0.14@\text{N-rGO}$ electrode exhibits excellent stability during the long-term electrolysis test. The current density is stable at about 21.3 mA cm^{-2} without obvious decay. The FE remains essentially unchanged with $78 \pm 2\%$ for formate and $11 \pm 1\%$ for CO over 20 h (Fig. 6b). Thus, the total FE of formate and CO remains about 89%, demonstrating a good stability.

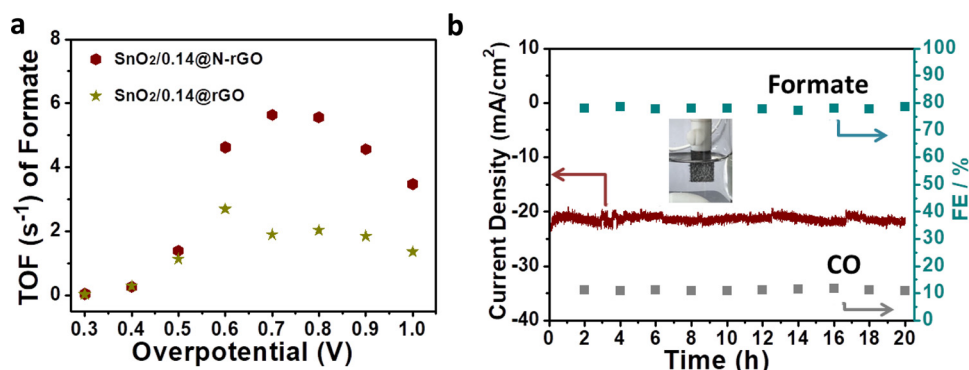


Fig. 6. (a) The TOF of formate formation for the $\text{SnO}_2/0.14@\text{N-rGO}$ and $\text{SnO}_2/0.14@\text{rGO}$ catalysts. (b) i - t curve, FE for formate and CO generation at the $\text{SnO}_2/0.14@\text{N-rGO}$ electrode in CO_2 -saturated 0.5 M NaHCO_3 solution (-0.8 V vs. RHE).

4. Conclusions

In summary, we have demonstrated the preparation of an efficient SnO₂@N-rGO catalyst consisted with ultrasmall SnO₂ nanocrystals and N-doped graphene via the facile combination of solution reaction and calcination. The as-prepared SnO₂@N-rGO electrocatalyst exhibits high activity, selectivity and long-term stability for the reduction of CO₂ to formate. Typically, a FE of 89% for formate and carbon monoxide formation at -0.8 V (vs. RHE) with a current density of ~21.3 mA cm⁻² has been achieved, which is comparable and even superior to most of the reported CO₂ reduction electrocatalysts. The enhanced performance would be attributed to the ensemble effect of nitrogen doping and SnO₂ nanocrystals on the surface of rGO sheets for favorable CO₂ adsorption, conversion, and stabilization of specific intermediates. This study opens up an exciting avenue to explore composite electrocatalysts by synthesizing the hybrids of metal oxides and heteroatom doped carbons for highly efficient CO₂ electroreduction.

Acknowledgement

This work was financially supported by the Natural Scientific Foundation of China (No. 21503116). Taishan Scholars Program of Shandong Province (No. tsqn20161004) and the Youth 1000 Talent Program of China are also acknowledged.

Appendix A. Supplementary data

Supplementary material related to this article can be found, in the online version, at doi:<https://doi.org/10.1016/j.apcatb.2018.08.044>.

References

- [1] K. Chang, T.F. Wang, J.G. Chen, *Appl. Catal. B* 206 (2017) 704–711.
- [2] Y.Z. Zhu, Z.X. Xu, Q.Q. Lang, W.Y. Jiang, Q.Q. Yin, S.X. Zhong, S. Bai, *Appl. Catal. B* 206 (2017) 282–292.
- [3] F. Lei, W. Liu, Y. Sun, J. Xu, K. Liu, L. Liang, T. Yao, B. Pan, S. Wei, Y. Xie, *Nat. Commun.* 7 (2016) 12697.
- [4] X. Gu, Z.H. Lu, H.L. Jiang, T. Akita, Q. Xu, *J. Am. Chem. Soc.* 133 (2011) 11822–11825.
- [5] M. Rezaei, S.H. Tabaian, D.F. Haghshenas, *Electrocatalysis* 5 (2014) 193–203.
- [6] S. Zhang, Y. Shao, G. Yin, Y. Lin, *Angew. Chem. Int. Ed.* 49 (2010) 2211–2214.
- [7] L. Fan, Z. Xia, M. Xu, Y. Lu, Z. Li, *Adv. Funct. Mater.* (2018) 1706289.
- [8] J.Q. Zeng, K. Bejtka, W.B. Ju, M. Castellino, A. Chiodoni, A. Sacco, M.A. Farkonrehfal, S. Hernández, D. Rentsch, C. Battaglia, C.F. Pirri, *Appl. Catal. B* 236 (2018) 475–482.
- [9] L. Wang, D. Wang, Z. Dong, F. Zhang, J. Jin, *Nano Lett.* 13 (2013) 1711–1716.
- [10] H. Seema, K.C. Kemp, V. Chandra, K.S. Kim, *Nanotechnology* 23 (2012) 355705.
- [11] S.Y. Jing, L.S. Zhang, L. Luo, J.J. Lu, S.B. Yin, P.K. Shen, P. Tsakarais, *Appl. Catal. B* 224 (2018) 533–540.
- [12] J.J. Wu, N. Li, X.H. Zhang, H.B. Fang, Y.Z. Zheng, X. Tao, *Appl. Catal. B* 226 (2018) 61–70.
- [13] P. Sekar, L. Calvillo, C. Tubaro, M. Baron, A. Pokle, F. Carraro, A. Martucci, S. Agnoli, *ACS Catal.* 7 (2017) 7695–7703.
- [14] Q. Li, W. Zhu, J. Fu, H. Zhang, G. Wu, S. Sun, *Nano Energy* 24 (2016) 1–9.
- [15] A.S. Varela, N.R. Sahraie, J. Steinberg, W. Ju, H.S. Oh, P. Strasser, *Angew. Chem.* 54 (2015) 10758–10762.
- [16] Z.S. Wu, W.C. Ren, D.W. Wang, F. Li, B.L. Liu, H.M. Cheng, *ACS Nano* 4 (2010) 5835–5842.
- [17] D. Gao, H. Zhou, J. Wang, S. Miao, F. Yang, G. Wang, J. Wang, X. Bao, *J. Am. Chem. Soc.* 137 (2015) 4288–4291.
- [18] B.H. Zhang, J.T. Zhang, *J. Energy Chem.* 26 (2017) 1050–1066.
- [19] Y. Yoon, A.S. Hall, Y. Surendranath, *Angew. Chem. Int. Ed.* 55 (2010) 15282–15286.
- [20] C.C. McCrory, S. Jung, I.M. Ferrer, S.M. Chatman, J.C. Peters, T.F. Jaramillo, *J. Am. Chem. Soc.* 137 (2015) 4347–4357.
- [21] M. Asadi, K. Kim, C. Liu, A.V. Addepalli, P. Abbasi, P. Yasaei, P. Phillips, A. Behranginia, J.M. Cerrato, R. Haasch, P. Zapoli, B. Kumar, R.F. Klie, J. Abiade, L.A. Curtiss, A.S. Khojin, *Science* 353 (2016) 467–470.
- [22] F. Li, J. Song, H. Yang, S. Gan, Q. Zhang, D. Han, A. Ivaska, L. Niu, *Nanotechnology* 20 (2009) 455602.
- [23] Y. Tang, D. Wu, S. Chen, F. Zhang, J. Jia, X. Feng, *Energy Environ. Sci.* 6 (2013) 2447–2451.
- [24] S. Oro, K. Urita, I. Moriguchi, *J. of Phys. Chem. C* 120 (2016) 25717–25724.
- [25] Y. Dong, Z. Zhao, Z. Wang, Y. Liu, X. Wang, J. Qiu, *ACS Appl. Mater. Interfaces* 7 (2015) 2444–2451.
- [26] Z. Zhu, S. Wang, J. Du, Q. Jin, T. Zhang, F. Cheng, J. Chen, *Nano Lett.* 14 (2014) 153–157.
- [27] K.Y.A. Lin, W.D. Lee, *Chem. Eng. J.* 284 (2016) 1017–1027.
- [28] I.V. Lightcap, T.H. Kosel, P.V. Kamat, *Nano Lett.* 10 (2010) 577–583.
- [29] X. Yu, Z.H. Zhao, D.H. Sun, N. Ren, J.H. Yu, R.Q. Yang, H. Liu, *Appl. Catal. B* 227 (2018) 470–476.
- [30] J. Duan, S. Chen, S. Dai, S.Z. Qiao, *Adv. Func. Mater.* 24 (2014) 2072–2078.
- [31] C. Zhang, B. Wang, X. Shen, J. Liu, X. Kong, S.S.C. Chuang, D. Yang, A. Dong, Z. Peng, *Nano Energy* 30 (2016) 503–510.
- [32] G. Tan, L. Chong, R. Amine, J. Lu, C. Liu, Y. Yuan, J. Wen, K. He, X. Bi, Y. Guo, H.H. Wang, R.S. Yassar, S.A. Hallaj, D.J. Miller, D. Liu, K. Amine, *Nano Lett.* 17 (2017) 2959–2966.
- [33] W. Peng, Z. Wang, N. Yoshizawa, H. Hatori, T. Hirotsu, *Chem. Commun. (Camb.)* 36 (2008) 4348–4350.
- [34] Y. Sun, F. Lei, S. Gao, B. Pan, J. Zhou, Y. Xie, *Angew. Chem. Int. Ed.* 52 (2013) 10569–10572.
- [35] J.T. Zhang, Z.G. Xiong, X.S. Zhao, *J. Mater. Chem.* 21 (2011) 3634–3640.
- [36] J.I. Lee, J. Song, Y. Cha, S. Fu, C. Zhu, X. Li, Y. Lin, M.K. Song, *Nano Res.* 10 (2017) 4398–4414.
- [37] B. Kumar, M. Asadi, D. Pisasale, S.S. Ray, B.A. Rosen, R. Haasch, J. Abiade, A.L. Yarin, A. Salehi-Khojin, *Nat. Commun.* 4 (2013) 2819.
- [38] F. Li, L. Chen, G.P. Knowles, D.R. MacFarlane, J. Zhang, *Angew. Chem. Int. Ed.* 56 (2017) 505–509.
- [39] S. Zhang, P. Kang, T.J. Meyer, *J. Am. Chem. Soc.* 136 (2014) 1734–1737.
- [40] D.H. Guo, R. Shibuya, C. Akiba, S. Saji, T. Kondo, J. Nakamura, *Science* 351 (2016) 361–365.
- [41] J.H. Koh, D.H. Won, T. Eom, N.K. Kim, K.D. Jung, H. Kim, Y.J. Hwang, B.K. Min, *ACS Catal.* 7 (2017) 5071–5077.
- [42] D.H. Won, C.H. Choi, J. Chung, M.W. Chung, E.H. Kim, S.I. Woo, *ChemSusChem* 8 (2015) 3092–3098.